Spin injection and accumulation in mesoscopic metal wires

2007 J. Phys.: Condens. Matter 19 165215

(http://iopscience.iop.org/0953-8984/19/16/165215)

IOP PUBLISHING JOURNAL OF PHYSICS: CONDENSED MATTER

J. Phys.: Condens. Matter **19** (2007) 165215 (18pp) doi:10.1088/0953-8984/19/16/165215

Spin injection and accumulation in mesoscopic metal wires

Mark Johnson

Naval Research Laboratory, Washington, DC 20375, USA

Received 22 September 2006
Published 6 April 2007
Online at stacks.iop.org/JPhysCM/19/165215

Abstract

Studies of spin injection, accumulation and detection in mesoscopic metal channels have recently gained considerable attention. The experiments use a nonlocal, quasi-one dimensional geometry and a structure that is known as a lateral spin valve. Results are interesting from the perspective of basic research and, of more importance, are promising for device applications. This article reviews the fundamentals of the theory and phenomenology of spin injection, describes novel data on mesoscopic silver wires with low ferromagnet/nonmagnet interface resistance, and discusses several important results. The plausibility of an optimized lateral spin valve, with output impedance of 50 Ω, output modulation of 10 Ω, and 50 nm dimensions, is analysed.

1. Introduction

Digital semiconductor electronics and magnetic storage are the two leading technology industries that motivate basic and applied research in condensed matter physics. Semiconductor electronics, the larger of the two, is based on complementary metal oxide semiconductor (CMOS) technology, which is built around the MOS field effect transistor (MOSFET). Since its invention in 1960 [1], the MOSFET has been the central device for both information processing and dynamic random access memory (RAM). This device will continue to be at the core of semiconductor technology for at least another decade, and its dominance shapes research in the field. While there is some basic research, for example related to advanced materials, applied research on topics associated with speed, size scaling, and power economy is extensive.

Unlike the semiconductor industry, magnetics technology looks to the future with considerable uncertainty. The basic device at the core of the industry has changed several times over the last decade. The read/write head is the component that determines the rate of development of the technology. In the past ten years, the device structure that was used for reading has been a sensor based on (i) anisotropic magnetoresistance (AMR), (ii) giant magnetoresistance (GMR), and most recently (iii) tunnel magnetoresistance (TMR). The technological lifetime of a given device structure has been short, and the device that will be

used in read heads a few years from now is not yet known. This competition and uncertainty presents an extraordinary opportunity for research. Wide-ranging basic research is supported, in particular with the goal of understanding the basic physics of spin transport in novel structures. At the same time, applied research is invaluable for determining the relevant device characteristics and the performance limits of any given structure.

The technological importance of studies of spin transport in structures composed of ferromagnetic and nonmagnetic materials was established several decades ago. Tedrow and Meservey [2] demonstrated that a spin-polarized current inside a thin ferromagnetic film could tunnel across a barrier and the polarization could be measured by tunnel conductance spectroscopy with reference to a superconducting counterelectrode. This demonstration of spin-dependent tunnelling (SDT) paved the way for the invention of the magnetic tunnel junction (MTJ) by Julliere [3]. With recent device advances [4], the MTJ has become a highly reliable and sensitive magnetic field sensor and has been used in commercial read heads since 2005. It can also be designed to have excellent characteristics as a storage cell in a nonvolatile magnetic random access memory (MRAM) [5].

The spin injection experiment [6, 7] demonstrated that spin-polarized current could be injected across a ferromagnet/nonmagnet (F/N) interface and that a nonequilibrium population of spin-polarized electrons (a spin accumulation) could diffuse into N over a large length scale. This experiment also demonstrated a resistance modulation in an $F1/N/F2$ sandwich structure that depended on the relative magnetization orientations, $M1$ and $M2$. It was followed by the discovery of giant magnetoresistance (GMR) [8], and the development of the current-in-plane (CIP) spin valve [9] and the current-perpendicular-to-the-plane (CPP) spin valve [10]. The study of devices in which electronic transport properties (current, voltage, or resistance) are modulated by the magnetization orientation of one or more device components has become known as the field of magnetoelectronics or spintronics.

Important developments in applied research, in particular relating to read-back techniques, occurred in parallel with the discoveries described above. Inductive read heads were replaced by magnetoresistive readers that utilized the anisotropic magnetoresistance (AMR) of a thin ferromagnetic film in 1992 [11]. These AMR read heads had relative magnetoresistance modulations, $\Delta R/R$, of about 4%. Within a few years, improvements in spin valves [12] resulted in properties far superior to AMR films, and CIP spin valves were used as sensors in read heads from 1999 to 2005. The period 1999 to the present has been one of remarkable success for the magnetic recording industry. The advances in read head technology have permitted areal storage density increases of roughly 100% per year, on average. This rate is higher than Moore's law for semiconductor electronics, 100% in 1.5 years.

The success of the magnetic recording industry has motivated efforts to expand magnetoelectronics technology to integrated electronics applications, directly challenging semiconductor technology. These efforts have focused on nonvolatile, magnetic random access memory (MRAM) as a target application [13]. Prototype MRAM chips have shown significant performance advantages over other nonvolatile memory technologies [5]. MRAM for embedded applications will likely be an entry point for integrated magnetoelectronics technology. Further improvements of magnetoelectronic devices will permit broader commercial penetration as high performance memory and, perhaps, reprogrammable logic [14].

As the magnetics industry looks to the future, there is continuing debate over the relative merits of several competing magnetoelectronic devices. Different devices have unique advantages, and face different challenges, as dimensions are shrunk to the range of tens of nanometres. CIP spin valves have relatively low impedance, relatively low magnetoresistive modulation $\Delta R/R$, and relatively low output voltage ΔV. Magnetic tunnel junctions (MTJs) have high $\Delta R/R$, but the device resistance R at small feature sizes is quite high and the

capacitance C is not negligible. This results in a slow RC time and a poor impedance match to other circuitry. CPP spin valves have higher $\Delta R/R$ than CIP spin valves and are believed to scale well at small dimensions. Spin injection and accumulation devices, which typically use a nonlocal geometry and are often called 'lateral spin valves', are characterized by a very low baseline resistance R and reasonable values of ΔR. This can be an advantage in applications for which $\Delta R/R$ is the operational figure of merit. In other applications, the modulation voltage ΔV is most important.

Spin accumulation has been predicted to scale inversely with the volume occupied by the nonequilibrium spin [6, 7]. This inverse scaling has been demonstrated over approximately ten decades and is an attractive feature of the lateral spin valve. Devices with lateral dimensions of roughly 100 nm have demonstrated ΔR values of about 1 Ω [15]. Another advantage of the lateral spin valve is that the output impedance is determined by the F/N junction resistance of the detection electrode, and high values of ΔR have been observed in devices with low interface resistance [16]. This means that the output voltage and output impedance are independent. Using inverse scaling along with an optimized interface resistance could result in a lateral spin valve with output transresistance of 10 Ω and output impedance of 50 Ω.

These recent advances have brought new focus to lateral spin valves, and have led to a resurgence of experiments on spin injection in mesoscopic metal samples [15–18]. This article reviews these results and discusses recent data on mesoscopic Ag device structures. Because the physics of spin injection and accumulation are somewhat different from that of GMR, we begin with a heuristic introduction of the concepts in section 2. Section 3 develops these ideas into rigorous theory, using both a microscopic transport model and a thermodynamic derivation. Section 4 gives a brief review of the first spin injection experiment, which introduced the lateral spin valve geometry along with the experimental transport measurement techniques that are still used. Recent experimental results on Ag are presented in section 5, and these are compared with other mesoscopic samples in section 6. Section 7 presents an analysis of spin transport characteristics, and a discussion of device merits is given in section 8.

2. Microscopic transport model of spin injection and accumulation

A microscopic transport model can be used to explain the basic physical principles of the lateral spin valve: electrical spin injection, nonequilibrium spin accumulation, and electrical spin detection [19]. A pedagogical geometry is shown in figure 1(a) along with simplified density of states diagrams to describe the transport processes (figure 1(b)). A bias current I driven through a single domain ferromagnetic film $F1$ and into a nonmagnetic metal sample N carries magnetization across the interface (with area A) and into N at the rate $J_M = \eta_1 \mu_B I/e$, where μ_B is the Bohr magneton and I/e is the number current. Here η_1 is the fractional polarization of carriers driven across the interface and is defined as the ratio $\eta_1 = (g_\uparrow - g_\downarrow)/(g_\uparrow + g_\downarrow)$, where $g_\uparrow$ and $g_\downarrow$ are the up- and down-spin subband conductances. The sample thickness d (figure 1(a)) is larger than an electron mean free path but smaller than a spin diffusion length, $d < \delta_s = \sqrt{DT_2}$, where T_2 is the spin relaxation time (in metals, the transverse spin relaxation time T_2 is the same as the longitudinal time, $T_2 = T_1$). In the steady state, J_M is the rate that magnetization is added to the sample region, and relaxation at the rate $1/T_2$ is steadily removing magnetization by spin relaxation and randomization. The resulting nonequilibrium magnetization,

$$\tilde{M} = I_M T_2/\mathrm{Vol}, \tag{1}$$

is a balance between these source and sink rates and is called *spin accumulation*. It represents a difference in spin subband chemical potential in N, $\tilde{M} \propto N_{n,\uparrow}(E_{F,n,\uparrow}) - N_{n,\downarrow}(E_{F,n,\downarrow})$ (figure 1(b)), and is depicted as grey shading in figure 1(a). In equation (1), the volume

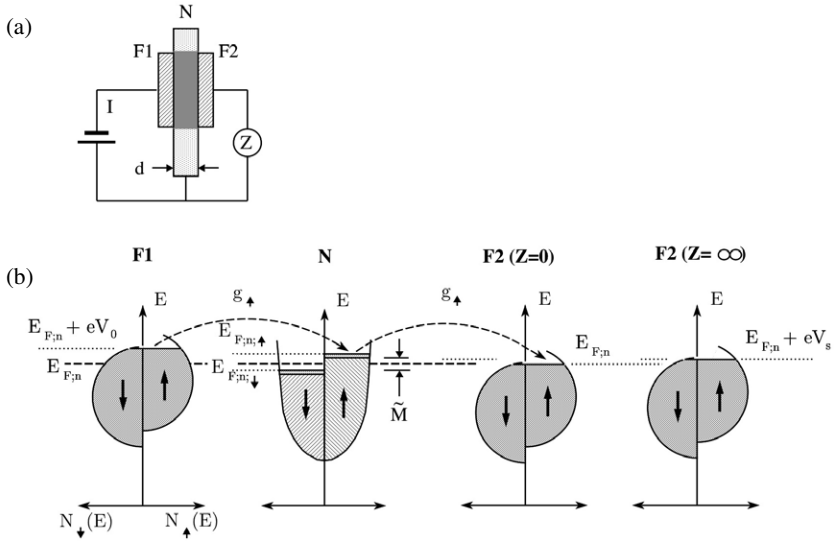

Figure 1. (a) Schematic cross-sectional sketch of the geometry of a pedagogical spin injection experiment. (b) Density of states diagrams to describe the microscopic transport model of the spin injection/accumulation/detection experiment in (a).

Vol $= A \cdot d$ is the volume occupied by the nonequilibrium spins. Magnetization $\tilde{M}$ is dimensionally correct, having units of magnetic moment per volume.

A second ferromagnetic film $F2$ that is in interfacial contact with the sample region acts as a spin detector. When connected to ground through a low impedance current meter ($Z = 0$ in figure 1(a)), a positive current $I_d \propto N_n(E_{F,n,\uparrow}) - N_n(E_{F,n})$ (where $E_{F,n}$ is the average chemical potential of the two spin subbands) is driven across the $N/F2$ interface and through the current detector when the magnetizations M_1 and M_2 are parallel. When M_1 and M_2 are antiparallel, the current $I_d \propto N_n(E_{F,n,\downarrow}) - N_n(E_{F,n})$ is negative. Conceptually, this induced electric current is the converse of the injection process and is an interface effect: a gradient of spin subband electrochemical potential across the $N/F2$ interface causes an interfacial electric field that drives an electrical current, either positive or negative depending on the sign of the gradient, across the interface. This is an emf source and current conservation demands that a clockwise (counterclockwise) current must be driven in the detecting loop.

If $F2$ is connected to ground through a high impedance voltmeter ($Z = \infty$ in figure 1(a)), then a positive (negative) voltage

$$V_s = \frac{\eta_2 \mu_B}{e} \frac{\tilde{M}}{\chi}, \tag{2}$$

is developed at the $N/F2$ interface [6, 19] when M_1 and M_2 are parallel (antiparallel). Here η_2 is the fractional polarization efficiency of the $N/F2$ interface and χ is the Paul susceptibility. The voltage V_s is directly related to the interfacial, spin subband electrochemical potential gradient described above. The expression for V_s can be combined with that for the magnitude of $\tilde{M}$, equation (1), to give the spin-coupled transresistance R_s that is observed in a spin injection/detection experiment. In the pedagogical geometry of figure 1(a), $\tilde{M}$ is confined to a volume Ad and the transresistance is [20]

$$R_s = \eta_1 \eta_2 \frac{\rho \delta_s^2}{\text{Vol}} = \eta_1 \eta_2 \frac{\rho \delta_s^2}{Ad}. \tag{3}$$

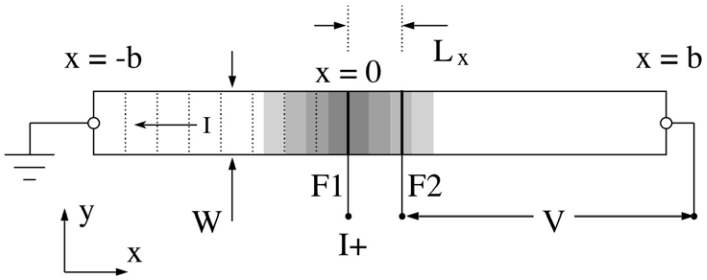

Figure 2. Schematic top view of a lateral spin valve. This nonlocal, quasi-one-dimensional geometry was introduced in the original spin injection experiment, and is used in mesoscopic metal wire samples. Dotted lines represent equipotentials characterizing electrical current flow. Grey shading represents the diffusing population of nonequilibrium spin-polarized electrons injected at $x = 0$, with darker shades corresponding to higher density of polarized electrons.

The experiments reviewed in this article all use a four-probe measurement with a quasi-one-dimensional metal wire in an unconfined geometry, as sketched with a top view in figure 2. For convenience, the wire can be chosen to lie along the $\hat{x}$ axis and to have a cross-sectional area A. Ferromagnetic electrodes $F1$ and $F2$ typically cross the N wire near the middle. Spin-polarized electrons injected at the $F1/N$ interface, at $x = 0$, diffuse into N along the $\hat{x}$ axis. Diffusion is equal for $x > 0$ and $x < 0$ [6, 21], and $\tilde{M}$ diminishes exponentially as the distance $|x|$ to the injector increases. The approximate volume occupied by the nonequilibrium spin population is $2A\delta_s$, where the factor of 2 comes from the length of a spin depth on both the positive and negative sides of $x = 0$. For a detector $F2$ located at a separation L from the injector, $L < \delta_s$, the transresistance is

$$R_s = \eta_1\eta_2\frac{\rho\delta_s}{2A}. \tag{4}$$

For a detector $F2$ located at a separation from injector $L > \delta_s$, the transresistance is [20]

$$R_s = \eta_1\eta_2\frac{\rho\delta_s}{2A}e^{-L/\delta_s}. \tag{5}$$

Experimentally, an in-plane magnetic field that flips the magnetizations $\vec{M}_1$ and $\vec{M}_2$ between parallel and antiparallel can be used to measure spin accumulation. Magnetoresistive dips appear between the coercive field values and the resistance difference is $\Delta R = 2R_s$. In a second experimental technique, involving the Hanle effect, $\tilde{M}$ is destroyed by application of an external, perpendicular magnetic field, $H_\perp$ [6, 7]. The amplitude of the field feature, $\Delta V(H_\perp)$, is proportional to the spin-coupled voltage of the accumulated spins, $\Delta V(H_\perp) \propto \tilde{M} \propto T_2$.

3. Johnson–Silsbee thermodynamic theory

Recognizing that gradients of nonequilibrium magnetization $\tilde{M}$ can drive currents of spin and charge across metal–metal interfaces, Johnson and Silsbee developed a thermodynamic theory [22] that can be used to derive the equations of motion of charge and spin in F/N systems. These are particularly useful for understanding interface effects, such as spin injection with a 'resistance mismatch' or across a tunnel barrier. The formal approach uses an entropy production calculation, where a *flux* J_N of a thermodynamic parameter N (charge, heat, and nonequilibrium spin magnetization) is associated with a generalized force, or affinity, F_N (gradients of voltage, temperature, magnetization potential). Each flux can, in general, be driven by each of the generalized forces, so that J_N can be expanded in powers of the F_N. Only

the first-order terms are kept for linear response theory, and the coefficients are known as the kinetic coefficients L_{mn}.

To summarize the derivation, electronic transport inside a bulk conductor, either ferromagnetic or nonmagnetic, is given by the linear dynamic transport equations [22]:

$$\begin{pmatrix} \mathbf{J_q} \\ \mathbf{J_Q} \\ \mathbf{J_M} \end{pmatrix} = -\sigma \begin{pmatrix} 1 & \frac{a''k_B^2T}{eE_F} & \frac{p\mu_B}{e} \\ \frac{a''k_B^2T^2}{eE_F} & \frac{a'k_B^2T}{e^2} & p'\frac{\mu_B}{E_F}\left[\frac{k_BT}{e}\right]^2 \\ \frac{p\mu_B}{e} & p'\frac{\mu_BT}{E_F}\left[\frac{k_B}{e}\right]^2 & \zeta\frac{\mu_B^2}{e^2} \end{pmatrix} \begin{pmatrix} \nabla V \\ \nabla T \\ \nabla -H^* \end{pmatrix}. \tag{6}$$

The kinetic coefficients $L_{m,n}$ can be provided phenomenologically, or estimated within a specific transport model. For example, $L_{1,3} = L_{3,1} = p_f(\mu_B/e)$ describes the flow of a magnetization current associated with an electric current in a ferromagnet, with fractional polarization p_f. Values of p_f are $p_f \approx 0.35$–0.45, according to experimental measurements [23]. Note that $L_{3,3} = \zeta(\mu_B/e)^2$ describes self-diffusion of nonequilibrium spins, and $\zeta \approx 1$ is an excellent approximation. In most cases, gradients and differences of temperature are small, heat flow is minimal, and all terms except $L_{1,1}$, $L_{3,1}$, $L_{1,3}$, and $L_{3,3}$ are negligible. Similar equations are derived for the discrete case of two metals separated by an interface with intrinsic electrical conductance G.

Driven by a gradient of voltage, the currents of charge and of polarized spins inside a nonmagnetic material are given by equations (6):

$$\mathbf{J_q} = -\sigma\nabla V \tag{7}$$

$$\mathbf{J_M} = -\sigma(p_n\mu_B/e)\nabla V = 0, \tag{8}$$

where $p_n = 0$ in a nonmagnetic material: there is no current of polarized electrons associated with an electric current in a nonmagnetic material. Spin-polarized currents may, however, exist in N. The currents of spin-polarized electrons are driven by self-diffusion and the $L'_{3,3}$ term of equations (6),

$$\mathbf{J_M} = -\sigma\mu_B^2/e^2\nabla(-H^*). \tag{9}$$

3.1. Detailed model of an F/N interface

The Johnson–Silsbee thermodynamic theory can be used to provide a detailed description of charge and spin transport across a F/N interface. Referring to figure 3(a), a ferromagnetic metal F and nonmagnetic material N are in interfacial contact. Considering isothermal flow, a constant current J_q is imposed and the solution for the resultant magnetization current J_M is calculated. Equations (6) are used to relate currents to potential gradients and to describe steady state flows in each of the materials F and N. The analogous discrete equations are used to relate interfacial currents with differences of potential across the interface. Boundary conditions demand that the magnetization currents of all three regions are equal at the interface ($x = 0$), $J_{M,f} = J_M = J_{M,n}$ (where J_M is the interfacial magnetization current), and that the electric currents are also equal, $J_{q,f} = J_q = J_{q,n}$.

In the general case, the flow of J_M into N generates a spin accumulation, $-H^* = \tilde{M}/\chi$, in N (figure 3(b)), and $-H^*(x)$ decreases as x increases away from the F/N interface. The nonequilibrium spin population can also diffuse *backwards*, along $-x$, going back across the F/N interface and into F. The nonequilibrium population $-H^*$ in F is not constrained to match that in N, $-H_f^*(x = 0) \neq -H_n^*(x = 0)$ (figure 3(b)) because, for example, the susceptibilities χ_f and χ_n can be quite different.

The backflow of diffusing, spin-polarized electrons must be overcome by the imposed current. The interface has some intrinsic resistance, $R_i = 1/G$, and the backflow acts as an

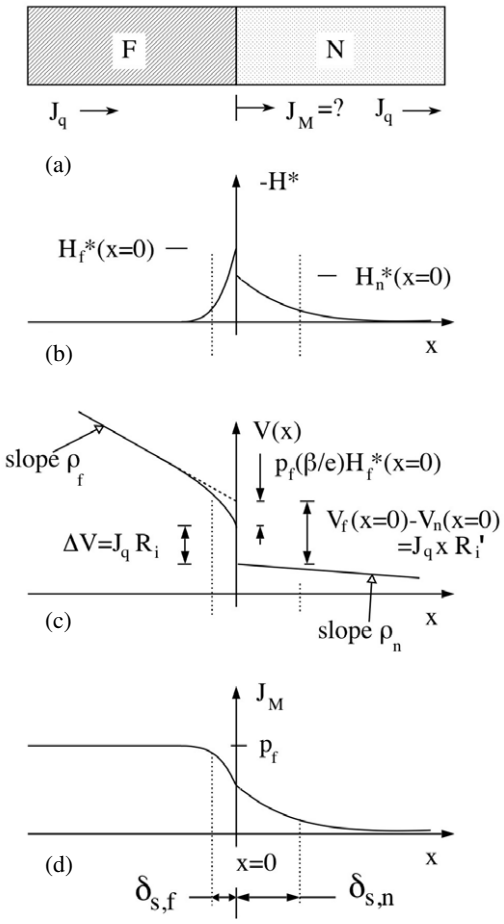

Figure 3. (a) Model for flow of charge and spin currents, J_q and J_M, at the interface between a ferromagnetic metal and nonmagnetic material. $x = 0$ at the interface. (b) Magnetization potential. The nonequilibrium spin population decays in F and N with characteristic lengths $\delta_{s,f}$ and $\delta_{s,n}$, respectively. (c) Voltage. (d) Current of spin magnetization, J_M.

additional, effective interface resistance (figure 3(c)). The spatial extent of the backflow is described by the spin diffusion length in F, $\delta_{s,f}$. An estimate for transition metal ferromagnetic films is $\delta_{s,f} \approx 15$ nm [16]. The backflow of polarized spins near the F/N interface effectively cancels a portion of the forward flowing polarized current $J_{M,f}$. The result is that the fractional polarization of the magnetization current that reaches and crosses the interface, J_M, is reduced relative to the bulk value, $J_M < J_{M,f}$ (figure 3(d)). This reduction of polarization arises from the L_{33} self-diffusion term in equation (6).

After algebraic manipulation, a general form for the interfacial magnetization current is found to be [21, 22]

$$J_M = \frac{\eta \mu_B}{e} J_q \left[\frac{1 + G(p_f/\eta) r_f (1-\eta^2)/(1-p_f^2)}{1 + G(1-\eta^2)\left[r_n + r_f/(1-p_f^2)\right]} \right], \tag{10}$$

where $r_f = \delta_f \rho_f = \delta_f/\sigma_f$, $r_n = \delta_n \rho_n = \delta_n/\sigma_n$, $G = 1/R_i$. It is important to note that spin transport is governed by the relative values of the intrinsic interface resistance, $R_i = 1/G$,

the resistance of a length of normal material equal to a spin depth, r_n, and the resistance of a length of ferromagnetic material equal to a spin depth, r_f. Typical values of these resistances are easily estimated; $r_f \sim 10^{-11}$ Ω cm^2 [16], $r_n \sim 2 \times 10^{-11}$ to 2×10^{-10} Ω cm^2, and $R_i = R_c \approx 10^{-11}$ Ω cm^2 [16]. Since all of the characteristic values fall within a range of a factor of ten, all of the terms in equation (10) are important for the general case.

3.2. Resistance mismatch at an F/N interface

One limiting case of equation (10) is that of low interfacial resistance, $R_i \to 0$. An appropriate experimental system is a multilayer, current-perpendicular-to-the-plane (CPP) GMR sample grown in UHV [25]. In this case, $R_i \approx 3 \times 10^{-12}$ Ω cm$^2 \ll r_f$ may justify the high conductance approximation. Equation (10) reduces to the simpler form [22, 24]:

$$J_M = p_f \frac{\mu_B}{e} J_q \left[\frac{1}{1 + (r_n/r_f)(1 - p_f^2)} \right]. \tag{11}$$

The polarization of the injected current is reduced from that in the bulk ferromagnet by the *resistance mismatch* factor $(1 + M')^{-1} = [1 + (r_n/r_f)(1 - p_f^2)]^{-1}$. Using the above estimates for r_f and r_n, the mismatch factor can be expected to be as large as $M' \sim 20$.

Another limiting case, that of high interfacial resistance, is depicted in figure 4. Spin accumulation in N can be large (figure 4(b)), but the resistive barrier prevents back-diffusion. The nonequilibrium spin population in F remains small, and the voltage drop across the interface is almost entirely due to R_i. The interfacial magnetization current is now given by

$$J_M = \eta \frac{\mu_B}{e} J_q, \tag{12}$$

and the fractional polarization is dominated by the interface parameter η. The resistive barrier may be asymmetric with respect to spin. For example, spin-up (or spin-down) electrons may have preferential transmission. The reflection of polarized carriers can diminish the polarization of current in F as it approaches the interface and, in general, the limit $\eta \leqslant p_f$ is imposed (figure 4(d)).

The general idea of 'resistance mismatch' has caused considerable confusion during the last few years. For example, a claim that 'resistance mismatch' was a fundamental obstacle [26] that would prevent spin injection across a ferromagnetic metal/semiconductor interface was based on a calculation using the infinite interface conductance limit, equation (11). However, a ferromagnetic metal/semiconductor interface is always characterized by a Schottky barrier, tunnel barrier, or low conductance 'ohmic contact'. In each case, the intrinsic interface resistance is high. Application of the infinite conductance approximation for a system that always has substantial interfacial resistance is fundamentally incorrect.

Rashba has used a tunnelling calculation to show that 'resistance mismatch' effects disappear when transport across a ferromagnet/semiconductor interface is mediated by a resistive barrier [27]. The resulting form for the fractional polarization of injected current agrees with equation (10) within factors of order unity. Thus, calculations based on nonequilibrium thermodynamics and those based on tunnelling formalism are in agreement. Any resistance which creates a voltage drop that blocks the backflow of polarized spins will permit efficient spin injection across the interface. The oversimplified resistance mismatch calculation [26] has been incorrectly applied to numerous experimental systems. It is important to realize that the condition $R_i \ll r_f, r_n$ is almost never realized and the general expression, equation (10), should be used. There are many experimental conditions, however, that justify the use of the form for high interface resistance, equation (11).

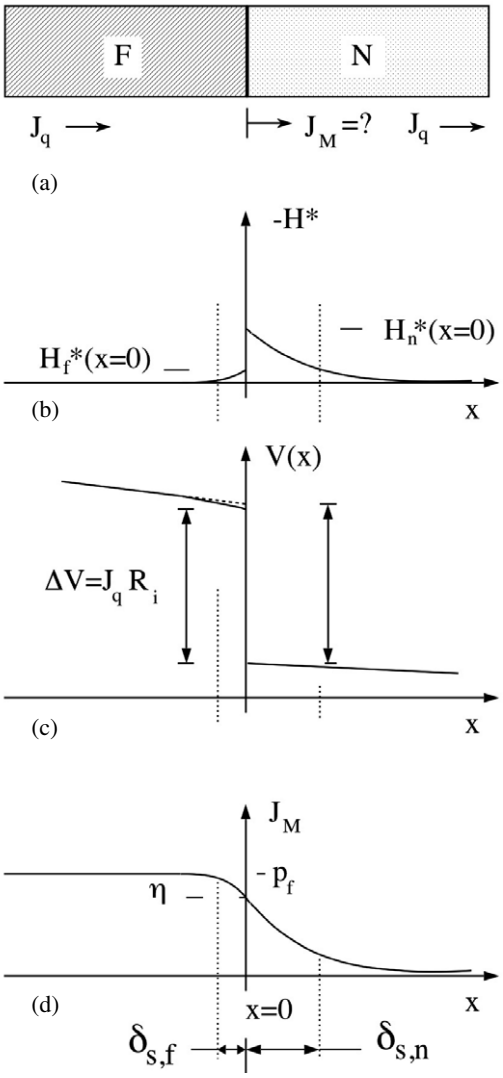

Figure 4. (a) Flow of charge and spin currents at an F/N interface, for the case of high intrinsic interface resistance, R_i. This case is relevant, for example, to cases of nonzero contact resistance, R_c, or tunnel barrier resistance R_b. (b) Magnetization potential. (c) Voltage. (d) Current of spin magnetization.

3.3. Spin dephasing and nonresonant transmission electron spin resonance (TESR)

As discussed above in section 2, in-plane magnetic fields can be used to make magnetoresistance measurements of R_s, and this is the relevant technique for device applications. However, another experimental technique for observation of spin accumulation is demonstration of the Hanle effect [6, 7, 17], the zero-frequency analogue of transmission electron spin resonance (TESR). In a simple picture, spin-polarized electrons diffuse across a distance L from the injector to the detector. Under the influence of a perpendicular magnetic field, each spin precesses by a phase angle that is proportional to the time it takes to reach the detector. Since the electrons are moving diffusively, there is a distribution of arrival times. In

the limit of zero external magnetic field, all the diffusing, polarized electrons that reach the detector have the same phase, as long as they have spent a time less than T_2 in the sample. For sufficiently large field, the spin phase angles of the electrons reaching the detector at any one time are completely random. If T_2 is increased, there is a larger distribution of arrival times at the detector, and a very small field is needed to randomize the distribution of phases. The characteristic field B_{hw} is given by the condition that the product of the precessional frequency and T_2 is a complete phase rotation angle of 2π. Thus, the characteristic field is $B_{hw} = 1/\gamma T_2$, where γ is the gyromagnetic ratio for electrons. It is explicit, in this inverse relationship, that long values of T_2 result in narrow lineshapes of the Hanle effect. Experimentally, the advantage of using the Hanle effect is that a single measurement gives relaxation time T_2 from the width of the Hanle feature, and polarization η is then the sole parameter to be fitted to the amplitude of the feature.

4. Experiments: spin injection in bulk samples

According to equations (1) and (3), both the spin accumulation and the transresistance of a spin injection device are inversely proportional to the volume occupied by the nonequilibrium spins. In the lateral spin valve, the relevant volume is defined by the product of the wire width, w, thickness, d, and the spin depth, δ_s. It has been observed that δ_s is the same order as the characteristic transverse dimension, $l \sim w$, and it follows that R_s scales roughly as $R_s \propto l^{-3}$. This inverse scaling is a highly promising device characteristic, and lateral spin valves may become competitive with semiconductor devices, for some applications, when the minimum feature size f becomes less than 50 nm. Understanding the limits of inverse scaling, which is crucially important to device viability, is a key topic of this article that will be discussed in section 7. One reason to review the first spin injection experiments, on bulk samples with large dimensions, is that they offer a pedagogical demonstration of the theoretical concepts. A second reason is that the quantitative results will provide a baseline for testing the inverse scaling rule by comparison with the recent results on mesoscopic structures.

The first spin injection experiment was performed on a 'wire' of bulk, high-purity aluminium, $w = 100$ μm and $d = 50$ μm [6, 7]. An array of ferromagnetic films, about 15 μm wide by 45 μm long, was fabricated by photolithography and liftoff as electrodes on the top surface, with interprobe spacings L_x in multiples of 50 μm. The F films were deposited by an electron beam from a single source of $Ni_{0.8}Fe_{0.2}$ in a pressure of 10^{-6} Torr after cleansing the Al surface with an Ar ion mill. These experiments introduced the nonlocal, lateral spin valve geometry (figure 2).

Spin injection, detection and accumulation are quantitatively measured by the Hanle effect (section 3.3). An example from an Al wire sample is shown in figure 5, presented in units of resistance, $R = V/I$. The lineshape is absorptive in appearance, and is described as a Lorentzian, when the injector and detector have magnetization orientations that are parallel. In general, the orientations $M1$ and $M2$ may not be exactly parallel. The Hanle data are then fitted to a mixture of absorptive and dispersive contributions. The data of figure 5 were fitted in this way, using equations derived in [19]. The lineshape is primarily absorptive in appearance, with a small dispersive contribution, for this sample with $L_x = 50$ μm, $T = 21$ K. After parameter $T_2 = 7.0$ ns is deduced from the line shape, the sole fitting parameter η is found from the amplitude, $\eta = 7.5\%$.

Figure 6 shows magnetotransport data for the sample with $L_x = 300$ μm using in-plane fields $H = H_y$. As the field is swept along the easy axis of $F1$ and $F2$ from positive to negative values, there is no Hanle feature near $H = 0$ because the field is parallel to the orientation axis of the injected spins. The region -80 Oe $< H <$ 30 Oe represents the reorientation of

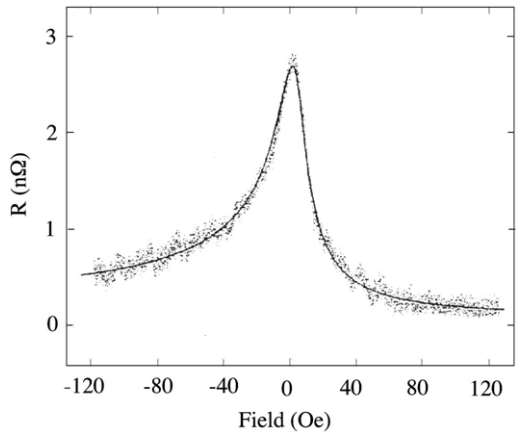

Figure 5. Example of Hanle data from bulk Al wire sample, presented in units of resistance as $R = V/I$. These data have an absorptive lineshape, with a small admixture of dispersive character. $L_x = 50\ \mu$m, $T = 21$ K. The solid line is a fit to the equations in [19]: $T_2 = 7.0$ ns, $\eta = 0.075$.

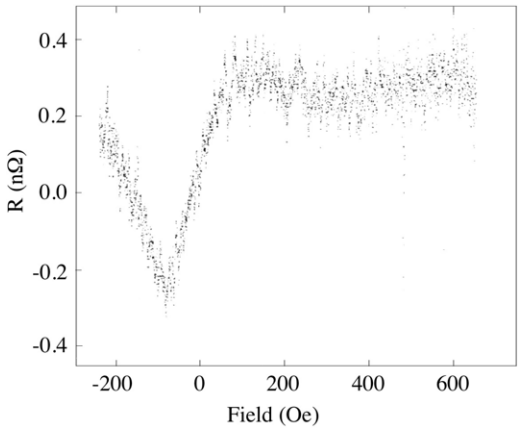

Figure 6. External field is applied along $\hat{y}$ axis, in the plane of $F1$ and $F2$, starting at $H_y = 600$ Oe, sweeping down and stopping at $H_y = -220$ Oe. The dip occurs when $\vec{M}_1$ and $\vec{M}_2$ change their relative orientation from parallel to antiparallel. By contrast with GMR, the resistive baseline is zero and the voltage IR_s is negative when $\vec{M}_1$ and $\vec{M}_2$ are antiparallel. A similar dip occurs for symmetric positive field when H_y is swept from negative to positive. $L_x = 300\ \mu$m, $T = 4.3$ K.

magnetizations $\vec{M}_1$ and $\vec{M}_2$ between parallel and antiparallel configurations, and the detected voltage V_s drops from positive to negative. In the region -200 Oe $< H < -80$ Oe the orientations $\vec{M}_1$ and $\vec{M}_2$ return to parallel and the original, positive voltage is regained. A field sweep from negative to positive values shows the same feature in the field range -80 Oe $< H < 200$ Oe, as expected for the hysteresis of the ferromagnetic films.

The magnitude of R_s, for a sample with $L_x \ll \delta_s$ (figure 5), is of the order of 1 nΩ at cryogenic temperatures. These samples had characteristic dimensions $l \sim 100\ \mu$m. The inverse scaling rule predicts that samples with dimensions $l \sim 100$ nm will have a transresistance of order 1 Ω. The experiments reviewed in the next two sections will show that this scaling is confirmed.

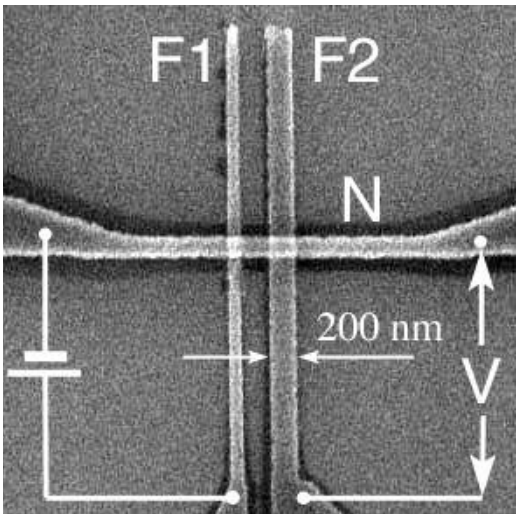

Figure 7. Scanning electron micrograph of mesoscopic spin injection device, in nonlocal geometry of figure 2. $F1$ and $F2$ are Permalloy with different widths. N is a Ag channel, having width of about 150 nm.

5. Experiments: spin injection in mesoscopic Ag wires

As noted in the introduction, there has been renewed interest in the topic of spin injection in thin film metal wires. The experiments typically involve mesoscopic samples in which the sample dimensions, w, d, and the separation L between injector and detector, are the order of, or smaller than, the electron mean free path ℓ in N. Since ℓ in disordered, nonmagnetic metal films is of the order of 100 nm, mesoscopic samples have a size scale relevant for device applications. All these recent experiments use the Johnson–Silsbee nonlocal, lateral spin valve geometry that is sketched in figure 2. At the Naval Research Laboratory, a set of experiments was performed on Ag wires. Silver was chosen for two reasons. First, spin injection had not been reported on this high-Z material, and measurements of the spin diffusion length offer new information about spin–orbit scattering. Second, silver does not readily oxidize and the F/N interface resistance can be controlled.

A scanning electron microscope image of a typical structure is shown in figure 7. Ferromagnetic electrodes $F1$ and $F2$ are both composed of Permalloy, formed using electron-beam deposition with a source of $Ni_{80}Fe_{20}$ in a vacuum with base pressure less than 10^{-7} Torr. The two electrodes were fabricated to have different coercivities that correlated with the different widths. In other samples, $F1$ was composed of Permalloy, $F2$ was composed of $Co_{90}Fe_{10}$, and the coercivities differed because of the different material properties. After the ferromagnetic electrodes were formed by electron-beam lithography (EBL) and liftoff, the sample was spun with a bilayer of resist. A pattern was exposed by EBL and developed. Prior to deposition of the Ag, the surfaces of the ferromagnetic electrodes was cleaned with an Ar ion mill. A 65 nm thick film of Ag was deposited by an electron beam, and the pattern was lifted off. The interface resistance was measured directly with crossing F/N wires that were fabricated on the same chips as the samples. The product of interface resistance R_i with junction area A, averaged over 5 junctions at 79 K, was 2.4×10^{-3} Ω μm^2, a value which increased by about 15% at room temperature. For a junction with median area of 90 nm by 190 nm, the interface resistance is $R_i = 140$ mΩ.

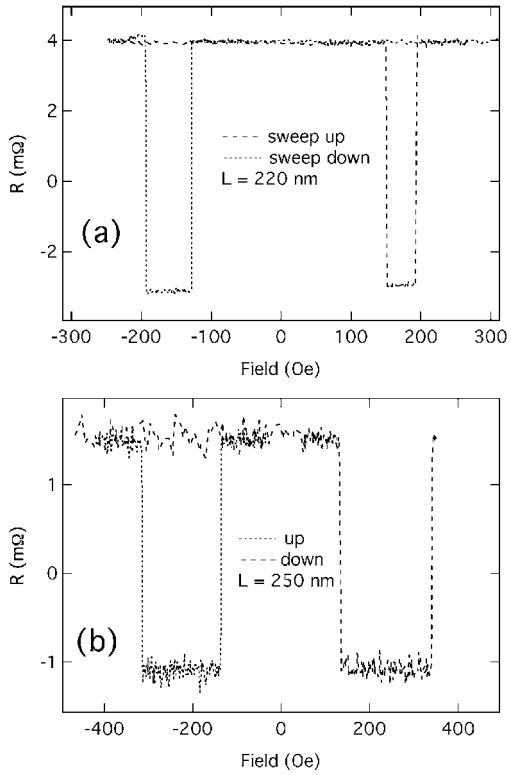

Figure 8. Examples of data from mesoscopic Ag samples. Dashed lines: field H is swept along $\hat{y}$ from negative to positive. Dotted lines: reverse sweeps. (a) Sample P97B2b. $F1$ and $F2$ are Permalloy. (b) Sample P90D2b. $F1$ is Permalloy and $F2$ is $Co_{90}Fe_{10}$. Compare with the data of figure 6, from a sample with volume larger by nine orders of magnitude.

Experiments were performed by using in-plane fields to manipulate the relative magnetizations M_1 and M_2 between parallel and antiparallel orientations to measure resistance dips, $\Delta R = 2R_s$. An example of data taken at 79 K, using an ac current bias at 35 Hz and a lock-in amplifier, is shown in figure 8(a). Sample P97B2b is similar to that shown in figure 7. The Ag film is 190 nm wide and the separation between injector and detector is $L = 220$ nm. The dashed trace corresponds to sweeping magnetic field H_y from -230 to $+230$ Oe. The magnetizations $\vec{M}_1$ and $\vec{M}_2$ are parallel for the field ranges $H_y < 140$ Oe and $H_y > 195$ Oe, and the resistance $R \approx +R_s = 4.0$ mΩ is a measure of the spin accumulation. In the field range 150 Oe $< H_y <$ 190 Oe, $\vec{M}_1$ and $\vec{M}_2$ are antiparallel, the resistance is $R \approx -R_s = -3.2$ mΩ, and the full amplitude of the resistance dip ΔR is $\Delta R = 2R_s = 7.2$ mΩ. In the dotted trace, the magnetic field is swept from $+300$ to -230 Oe, and the dip occurs at $H_y < 0$ because of hysteresis. The observed values $|\pm R_s|$ are nearly symmetric about $R = 0$ and the baseline resistance R_B of about 0.4 mΩ, nearly zero, confirms the effectiveness of the nonlocal geometry. Small differences from zero occur when the geometry deviates from ideal.

Figure 8(b) shows an example of data from sample P90D2b at $T = 79$ K. In this sample, $F1$ is Permalloy and $F2$ is $Co_{90}Fe_{10}$. The magnetization $M2$ switches at a higher field, $|H_y| \approx 350$ Oe, the field range where $M1$ and $M2$ are antiparallel is larger, and the

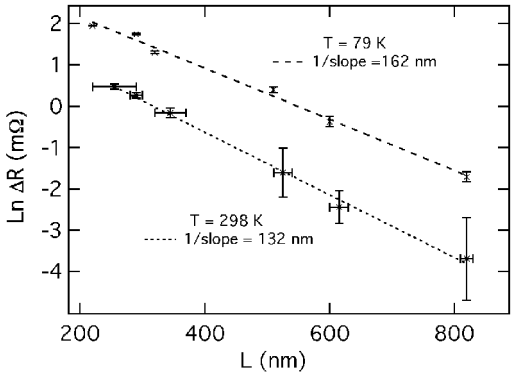

Figure 9. Semilog plots of $\Delta R(L)$ for sample P97B2b at $T = 79$ and 298 K, and fits. At 298 K, the relatively short spin depth causes an uncertainty in L, shown with error bars.

magnetoresistive dips are wider. For sample P90D2b, $w = 260$ nm, and η_{CoFe} is comparable with η_{NiFe}.

As discussed below, δ_{s} is sensitive to the resistivity ρ_{Ag} of the Ag, and ρ_{Ag} changes from sample to sample. To minimize this variation, samples were prepared with an array of four Py electrodes contacting each Ag wire. The widths, and therefore coercivities, of the four F wires were uniquely different. Using these in a variety of combinations of injector and detector permitted measurements for a variety of spacings L while the variation of ρ_{Ag} was measured to be small (typically $\pm 12\%$).

In these structures, spin-dependent scattering may occur at the F/N interface of any unused F electrode within δ_{s} of the injector. However, such scattering can be discounted as negligible for two reasons. First, several data sets were taken at a long injector–detector separation. Even though there is an intervening F electrode, these data show single dips in the up and down field sweeps. The baseline is flat, and there is no indication of a change in resistance that would indicate a change in $\tilde{M}$ caused by the magnetization reversal of the intervening electrode. Second, we have compared data for samples taken with two F electrodes with data from samples with intervening F electrodes. For comparable Ag resistivity and separation L, the dips ΔR are the same within experimental error. It follows that any effects of spin-dependent scattering at the N/F interface are negligible in our measurements.

For a given device set, the amplitude of R_{s} as a function of L, measured from $\Delta R(L)$, is fitted to equation (5) to find the spin diffusion length, δ_{s}. Plots of $\Delta R(L)$ for sample P97B2b at 79 and 298 K are shown in figure 9 along with their fits. From the measured spin depth $\delta_{\mathrm{s}} = \sqrt{DT_2}$, we use an Einstein relation $D = [e^2 \rho N(E_F)]^{-1}$ and a value for $N(E_F)$ from specific heat measurements [16] to solve for T_2. For example, for P97B2b with $\delta_{\mathrm{s}} = 162$ nm, we find $D = 93$ cm^2 s^{-1} and $T_2 = 2.8$ ps. The spin flip probability, $\alpha = \tau/T_2$, is calculated using a Drude time for τ deduced from ρ. Finally, equation (5) and the amplitude R_{s} are used to find the average fractional polarization η' for $F1$ and $F2$. Since all other parameters are measured directly, η' is the sole fitting parameter. The charge and spin transport parameters for several sample sets are summarized in table 1.

6. Experiments: spin injection in mesoscopic metal wires

Without discussing all of the work in this field, several interesting and important experiments can be reviewed. Mesoscopic Cu wires, of width 100 nm and thickness 54 nm, were fabricated

Table 1. Characteristic parameters for several Permalloy/Ag lateral spin valve samples.

Sample	T (K)	ρ ($\mu\Omega$ cm)	δ_s (nm)	T_2 (ps)	$\alpha = \tau/T_2$	η' (%)
C1b	79	3.5	195	3.5	0.0043	21 ± 1
B2b	79	4.0	162	2.8	0.0054	24
B2b	298	5.5	132	2.6	0.0043	12
B1b	79	3.8	189	3.6	0.0044	22
B1b	298	4.9	152	3.0	0.0040	12

with Co electrodes having slightly different widths, $w_1 = 95$ nm and $w_2 = 105$ nm, thickness 36 nm, and tunnel barriers [17]. The Hanle effect was used to measure a spin relaxation time $T_2 = 22$ ps (at 4 K), a fractional polarization of $\eta = 5.5\%$ was deduced, and the ratio $\tau/T_2 = \alpha_{Cu} = 0.000\,66$ was determined (4 K). The spin depth of $\delta_s = 550$ nm was confirmed by measuring $R_s(L)$, for a variety of values of L, with in-plane fields. These spin injection experiments in Cu also studied the temperature dependence of spin transmission across the $F/I/N$ junctions up to 295 K.

A second experiment was a study of spin injection in thin Al wires [15]. One F electrode was composed of FeCo and the other was Permalloy. The surface of the Al wire was oxidized before deposition of the F electrode, so that a tunnel barrier was incorporated at the interface between F and N. Measurements were made on samples with differing values of tunnel junction thickness and impedance. For the thinnest Al samples (6 nm thick, $w = 125$ nm), the spin depth was determined by measuring $R_s(L)$ for a variety of values of L, and was found to be $\delta_s = 200$ nm. This value was independent of temperature, suggesting that electron scattering was dominated by temperature-independent surface scattering. The fractional polarization was deduced from the magnitude of R_s. For tunnel junctions with impedance of order 1–10 kΩ, the largest value of η was $\eta = 25\%$ (averaged for the two different electrodes) at 4 K and $\eta \approx 16\%$ at 295 K. These values corresponded to very large amplitudes of $\Delta R = 2R_s$, larger than 2 Ω at 4 K and larger than 1 Ω at 295 K. From the published value for the resistivity of the 6 nm thick Al sample, $\rho = 3.3 \times 10^{-5}$ Ω cm, a spin relaxation time $T_2 = 48$ ps is calculated. This corresponds to a low value of $\alpha_{Al} = 1.3 \times 10^{-5}$, using a Drude time of $\tau = 6.4 \times 10^{-16}$ s.

A third experiment has reproduced the large value of ΔR observed in thin Al films [28] and, furthermore, it directly confirmed predictions of the Johnson–Silsbee model: spin currents in N are not coupled to electric currents but instead are driven by self-diffusion, and spin diffusion is isotropic [6, 21, 22]. On a 100 nm wide, 15 nm thick Al wire, ferromagnetic detectors were placed on either side of a ferromagnetic injector, at equal distances of $|L_x| =$ 300 nm. The aluminium was oxidized before deposition of the cobalt ferromagnetic electrodes, so that a tunnel barrier separated the F and N layers. The injected current was grounded at one end of the wire. The spin-dependent voltages of the two Co detecting films was compared and found to be equal. Since one of the detectors was along the current path and the other was in the 'nonlocal' portion of the wire, the equivalence of the spin-dependent voltages demonstrated that the spin accumulation diffused equally in both directions, independent of the electric current path. Quantitatively, the magnitude of ΔR was about 0.15 Ω. By analysing $\Delta R(L)$, a long spin diffusion length of $\delta_s = 850$ nm was measured at 4 K. The Al resistivity was low, $\rho = 4$ $\mu\Omega$ cm, and the authors deduced values $\eta = 12\%$ for their tunnel junctions, $T_2 = 110$ ps, and $\alpha = \tau/T_2 = 1 \times 10^{-4}$. Allowing for the different thickness of the Al wire and differing values of η, the magnitude of spin accumulation is quite comparable with that observed in [15].

7. Analysis and discussion

It is interesting to discuss these results in the context of three questions. (i) What can be learned about models of spin flip scattering from the measured values of α? (ii) Is there consistency between interface properties and the deduced values of η? (iii) What are the limits of the inverse scaling of spin accumulation?

In the original spin injection experiment [6, 7], the spin depth was found to be $\delta_s = 0.4$ mm at $T \sim 10$ K, and a typical spin relaxation time was $T_2 = 10$ ns. From the measured resistivity of the Al, a value $\alpha_{Al} = 0.0010$ was found. Values of η ranged from 4.5% to 8%, and $\Delta R = 2R_s$ ranged from 2 to 6 nΩ. These values provide a baseline for comparison with results in mesoscopic samples.

(i) The simplest interpretation of Yafet–Elliott spin–orbit interactions assumes that electron scattering from impurities, grain boundaries, phonons and sample surfaces is different in each case, and each is associated with a different spin scattering probability. This probability is generally considered to be roughly the same for all of these scattering mechanisms, but is assumed to scale in proportion with nuclear Z of the nonmagnetic material. For aluminium, values of α_{Al} deduced from experiments vary by two orders of magnitude. In the original experiment, on bulk samples, $\alpha_{Al} = 0.0010$ is the same as values measured by TESR on comparable samples, but is much larger than expected. Aluminium has a complicated Fermi surface and calculations showed that the spin scattering probability was very small over most of the Fermi surface but was very large in the vicinity of a few small regions [29]. Spin scattering at these 'hot spots' completely dominated all spin scattering events, and these calculations gave agreement with the experimental value, $\alpha_{Al} = 0.0010$.

The observation of a very small ratio, $\alpha_{Al} = 1.3 \times 10^{-5}$, in mesoscopic Al wires [15] suggests that the probability of spin scattering at surfaces may differ substantially from that for other events. These samples are so thin that surface scattering is assumed to dominate at all temperatures. The observed ratio of τ/T_2 is two orders of magnitude smaller than the value in bulk Al, and one order of magnitude smaller than the value $\alpha_{Al} = 1 \times 10^{-4}$ observed in [28], where the thin film Al samples are roughly twice as thick and eight times more conductive. A tempting explanation is that τ_{surf}/T_2, where τ_{surf} is a mean time for surface scattering, is much smaller than the ratio for other mechanisms. Further studies are required in order to show that the high resistivity of the Al film in [15] can be associated with surface scattering.

Recent experiments on mesoscopic Ag wires [16] observed a value $\alpha_{Ag} = 0.0045 \pm 0.001$, independent of temperature over the range from 77 to 295 K. This is roughly comparable with the value α_{Au} measured in two-dimensional Au films [30]. Simple application of Yafet–Elliott spin scattering would predict $\alpha_{Ag} < \alpha_{Au}$. However, if τ/T_2 varies for different scattering mechanisms, then variation in the observed value of τ/T_2 can be expected for different experiments and different sample geometries. The value $\alpha_{Cu} = 0.000\,66$ was measured in copper, and $\alpha_{Cu} < \alpha_{Ag}, \alpha_{Au}$ is consistent with the simple interpretation of Yafet–Elliott theory.

(ii) Values of η vary over a large range, but there is some consistency for comparisons between samples with comparable interfaces. For F/N tunnel junctions at low temperature, $\eta = 5.5\%$ was measured for Co/Cu samples [17], and $\eta = 15\%$–25% was measured for CoFe/Al samples [15]. The agreement is better at room temperature, $\eta = 12\%$ for Co/Al samples [28] and $\eta = 16\%$ for CoFe/Al. For low-resistance F/N junctions, $\eta = 25\%$ was measured for Co/Au junctions on mesoscopic Au wires [31], and $\eta = 22 \pm 1\%$ was measured for NiFe/Ag junctions on mesoscopic Ag wires. Given the large variation of values of η, details of the F/N interface must play a crucial role in determining the efficiency of spin transport.

Several important points can be noted. First, the reason that values of η observed in spin injection experiments are much smaller than the theoretical limit of $p_f = 0.4$–0.5 is not

yet understood. Second, the theoretical discussion of section 3.2 is experimentally validated. The condition $R_i \ll r_f, r_n$ is almost never realized, the general expression, equation (10), should be used, and the oversimplified resistance mismatch model [26] is not valid. Analysing the Permalloy/Ag experiments [16] with equation (10) predicts that increasing the interface resistance from the order of 0.1 Ω to roughly 10 Ω will increase η to a value near the theoretical maximum. Third, the temperature dependence of η, decreasing as temperature increases up to 295 K, may be explained by spin asymmetries in the injecting interface [17]. Achieving a high value of η at room temperature will require further theoretical understanding and careful interface engineering.

(iii) Inverse scaling of spin accumulation can be tested by comparing the spin transresistance observed in the original spin injection experiment with that measured on mesoscopic aluminium wires. The sample material is the same, and the comparison will be made at the same temperature, 4 K. The volume of the former, 2×10^{-6} cm^3 for a sample 100 μm by 50 μm and having $\delta_s = 400$ μm, is 10^{10} larger than that of the latter, 1.5×10^{-16} cm^3 for a sample 125 nm by 6 nm and having $\delta_s = 200$ nm. The transimpedance of the latter, $R_s = 1$ Ω, is 5×10^8 times larger than that of the former, $R_s = 2$ nΩ. The inverse scaling is maintained over ten decades within an order of magnitude, but this is somewhat fortuitous. Referring to equation (1), $\tilde{M}$ is inversely proportional to sample volume, but varies directly with spin relaxation time T_2. Since T_2 is proportional to the mean scattering time τ, $\tilde{M}$ and R_s are expected to diminish in structures where τ is limited by sample dimensions or material quality. The relatively large value of η in the mesoscopic aluminium samples compensates a portion of this decrease. The combined result is that inverse scaling is observed within a factor of 20.

8. Device applications

As the magnetics industry looks to future device generations, the leading application will continue to be the magnetic field sensor used in read–write heads. Integrated applications, such as MRAM, could have a large market impact if they can be cost competitive. For any application, future devices must have high performance at a feature size of 50 nm, and must scale favourably to smaller sizes. A successful device must be able to impedance match to 50 Ω, characteristic of on-chip circuitry. A resistance modulation of $\Delta R \approx 10$ Ω (at room temperature), resulting in an output voltage swing of a few mV for bias currents of a few tenths of a mA, is adequate for sensor and memory applications.

A lateral spin valve with characteristic size $l \approx 125$ nm, tunnel barriers, and an Al channel has $\Delta R = 1$ Ω (for $\eta = 15\%$) with an output impedance of about 10 kΩ [15]. Keeping the Al film thickness the same, reducing l to 50 nm would reduce the effective volume, and increase $\tilde{M}$, by a factor of four. The theoretical maximum value of η is about 45%, and a reasonable increase to $\eta = 30\%$ would increase $R_s \propto \eta^2$ by four. Therefore, a value $\Delta R = 16$ Ω is quite plausible. Of equal importance, the tunnel barrier is not necessary for efficient spin injection [16]. The $N/F2$ interface resistance, and therefore the output impedance, could be engineered for an optimal value of 50 Ω. With these plausible improvements, a lateral spin valve with highly desirable characteristics is an attractive possibility.

Acknowledgment

The author gratefully acknowledges the support of the Office of Naval Research, Award N0001405-AF00002.

References

[1] Kahng D and Atalla M 1960 *US Patent Specifications* 3,102,230 and 3,206,670
[2] Tedrow P M and Meservey R 1971 *Phys. Rev. Lett.* **26** 192
[3] Julliere M 1975 *Phys. Lett.* A **54** 225
[4] Ho M K, Tsang C H and Fontana R E 2001 *IEEE Trans. Magn.* **37** 1691
[5] Tehrani S *et al* 2003 *Proc. IEEE* **91** 703
[6] Johnson M and Silsbee R H 1985 *Phys. Rev. Lett.* **55** 1790
[7] Johnson M and Silsbee R H 1988 *Phys. Rev.* B **37** 5326
[8] Baibich M *et al* 1988 *Phys. Rev. Lett.* **61** 2472
[9] Binasch G *et al* 1989 *Phys. Rev.* B **39** 4828
[10] Bass J and Pratt W P Jr 1990 *J. Magn. Magn. Mater.* **200** 274
[11] Tsang C *et al* 1990 *IEEE Trans. Magn.* **26** 1689
[12] Dieny B *et al* 1991 *J. Appl. Phys.* **69** 4774
[13] Johnson M 1993 *Science* **260** 324
[14] Johnson M 2000 *IEEE Spectr. Mag.* **37** 33
[15] Valenzuela S O and Tinkham M 2004 *Appl. Phys. Lett.* **85** 5914
[16] Godfrey R and Johnson M 2006 *Phys. Rev. Lett.* **96** 136601
[17] Garzon S, Zutic I and Webb R A 2005 *Phys. Rev. Lett.* **94** 176601
[18] Ji Y, Hoffman A, Pearson J E and Bader S D 2006 *Appl. Phys. Lett.* **88** 052509
[19] Johnson M and Silsbee R H 1988 *Phys. Rev.* B **37** 5312
[20] Johnson M 1994 *J. Appl. Phys.* **75** 6714
[21] Johnson M and Byers J 2003 *Phys. Rev.* B **67** 125112
[22] Johnson M and Silsbee R H 1987 *Phys. Rev.* B **35** 4959
[23] Nadgorny B, Soulen R J, Osofsky M S, Mazin I I, LaPrade G, van de Veerdonk R J M, Smits A A, Cheng S F, Skelton E F and Qadri S B 2000 *Phys. Rev.* B **61** R3788
[24] Johnson M and Silsbee R H 1988 *Phys. Rev. Lett.* **60** 377
[25] Yang Q *et al* 1994 *Phys. Rev. Lett.* **72** 3274
[26] Schmidt G, Ferrand D, Mollenkamp L W, Filip A T and van Wees B J 2000 *Phys. Rev.* B **62** R4790
[27] Rashba E I 2000 *Phys. Rev.* B **62** 16267
[28] Urech M, Korenivski V, Poli N and Haviland D B 2006 *Nano Lett.* **6** 871
[29] Fabian J and Das Sarma S 1998 *Phys. Rev. Lett.* **81** 5624
[30] Johnson M 1993 *Phys. Rev. Lett.* **70** 2142
[31] Ku J-H, Chang J, Kim H and Eom J 2006 *Appl. Phys. Lett.* **88** 172510